Infill Optimization for Additive Manufacturing –Approaching Bone-like Porous Structures

Jun Wu, Niels Aage, Rüdiger Westermann, Ole Sigmund

Abstract—Porous structures such as trabecular bone are widely seen in nature. These structures are lightweight and exhibit strong mechanical properties. In this paper, we present a method to generate bone-like porous structures as lightweight infill for additive manufacturing. Our method builds upon and extends voxel-wise topology optimization. In particular, for the purpose of generating sparse yet stable structures distributed in the interior of a given shape, we propose upper bounds on the *localized* material volume in the proximity of each voxel in the design domain. We then aggregate the local per-voxel constraints by their *p*-norm into an equivalent global constraint, in order to facilitate an efficient optimization process. Implemented on a high-resolution topology optimization framework, our results demonstrate mechanically optimized, detailed porous structures which mimic those found in nature. We further show variants of the optimized structures subject to different design specifications, and we analyze the optimality and robustness of the obtained structures.

Index Terms—Infill, additive manufacturing, trabecular bone, porous structures, topology optimization.

1 Introduction

In additive manufacturing, which is also known as 3D printing, the term *infill* refers to the interior structure of an object that is printed. The infill often has a *regular* structure, which is selected by the user in the slicing software in addition to a specific volume percentage. The infill pattern and volume percentage significantly influence the printing process as well as physical properties of the printed object. In general, a higher volume percentage leads to a print that is more resistant to external loads while consuming more material and prolonging the print time. To assist users in designing lightweight *and* mechanically strong prints, i.e., to find infills that are further optimized regarding these properties, in this work we propose a new approach combining structural analysis and optimization.

Our approach is inspired by the architecture of bone. Bone is composed of two types of structures – compact *cortical bone* forming its outer shell, and spongy *trabecular bone* occupying its interior (see the cross section of a human femur in Fig. 1). This composite results from a natural optimization process during which the bone adapts itself to the mechanical load (Wolff's law [1]). As a consequence of this natural adaptation, micro-structures of trabecular bone are aligned along the principal stress directions. This is illustrated in the second image of Fig. 1. The resulting composition is lightweight, resistant, robust with respect to force variations, and damage-tolerant [2], [3]. These properties make bone-like structures an appealing option as infill for additive manufacturing.

In this paper we present a new approach for the generation of bone-like porous structures. This approach builds upon and extends the general, voxel-wise topology optimization scheme [6], [7]. It maximizes the mechanical stiffness by optimizing the distribution of a prescribed amount of material in a given design domain under a given set of external loads. In particular, to generate porous structures we propose a formulation to measure local volume fractions, and then impose constraints on such values in order to regulate the local material distribution. Under the objective function to maximize stiffness, the porous structures are automatically aligned to accommodate the mechanical loads in an optimized manner.

The specific contributions of our paper are:

- A novel formulation for generating porous structures firmly based on structural optimization.
- Insights into optimal structures from a mechanical perspective, analyzed via a detailed parameter study.

The remainder of this paper is organized as follows. After reviewing related work in Section 2, in Section 3 we present the problem formulation and the techniques for solving the infill optimization problem. In Section 4, we discuss extensions to steer the optimization process. Results and analysis are presented in Section 5, before conclusions are drawn in Section 6.

2 Related Work

In 3D printing, much research has been devoted to the modelling of geometric shapes with specific physical properties. In this section, we review techniques related to the optimization of mechanical properties. For a thorough overview of geometric and physical modeling approaches

- *Jun Wu, Niels Aage and Ole Sigmund are with the Department of Mechanical Engineering, Technical University of Denmark, Lyngby, Denmark.*
- *Rüdiger Westermann is with the Department of Computer Science, Technische Universität München, Munich, Germany.*
- *Corresponding Author: Jun Wu, E-mail: junwu@mek.dtu.dk*

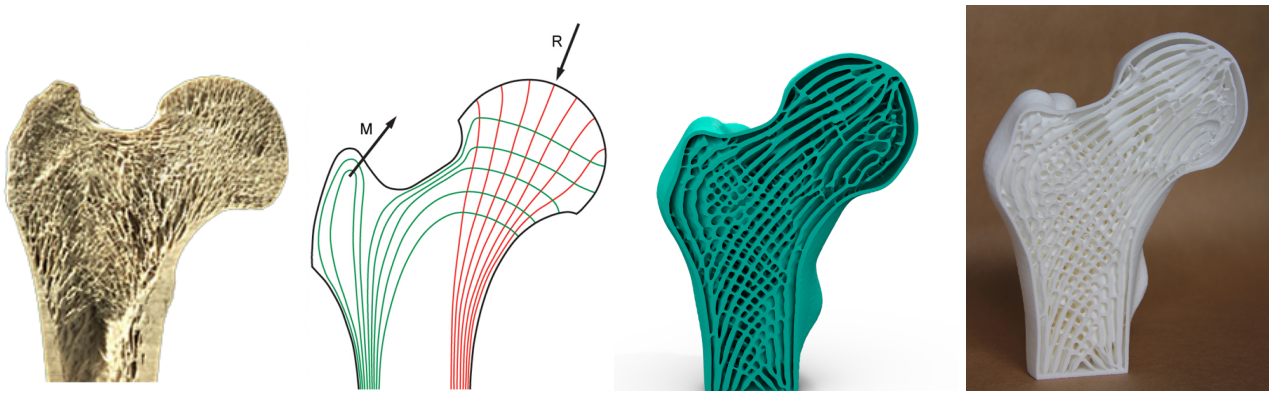

Fig. 1: From left to right: Cross-section of a human femur showing cortical structures on the shell and trabecular structures in the interior [4]. Illustration of principal stress directions under major mechanical loads [5]. Cross-section of the optimized porous infill in a 3D bone model. The 3D printed bone model.

for 3D printing, let us refer to the recent survey article by Gao et al. [8] and the tutorial by Liu eat al. [9].

Early work by Smith et al. [10] addressed the layout of truss structures for optimizing bridges and towers with respect to mechanical stiffness. Wang et al. [11] and Lu et al [12] respectively, introduced skin-frame structures and honeycomb-like Voronoi structures as lightweight composites for the shape interior. To assist users in the design of 3D printable shapes, Stava et al. [13] presented a system for detecting structural deficiencies by means of a finite element analysis. A set of correction operations including hollowing, thickening, and strut insertion was proposed to improve a shape's structural soundness. Zhou et al. [14] presented an efficient analysis to detect worst-case loads for stress and deformation criteria, making no assumptions on the placement of the forces. Manufacturing constraints regarding toolpath restriction and overhang avoidance were addressed by Zhao et al. [15] and Wu et al. [16], respectively. The assembly of shapes from manufacturable micro-structures has been investigated in computer graphics [17], [18], [19] and topology optimization (e.g., [20], [21], among others). Our work is inspired by these works, yet it avoids the use of prescribed micro-structures to generate structural compositions that are less limited in the mechanical properties they can achieve.

Topology optimization Topology optimization is based on a volumetric element-wise parametrization of the design domain. This general formulation does not prescribe the topology *a priori*, but allows structures to appear and adapt during the iterative optimization process. For a thorough review of topology optimization techniques let us refer to recent survey articles [22], [23]. Our work is based on the density approach, which is known as Solid Isotropic Material with Penalization (SIMP) [24]. The method is related to the length scale problem in the literature of topology optimization, where the interest is to control the minimal and/or maximal structure size for manufacturability [25], [26]. In particular, we follow the idea of the projection filter [27], [28] in our implementation to impose local volume constraints. Different from exact length scale control, we propose a projection method in an approximate manner to facilitate fast numerical solutions. In our work we employ the potential of numerical multigrid schemes to enable topology optimization at high resolution and efficiency [29].

Approaching bone-like structures While we approach bone-like porous structures for their superior mechanical properties by using topology optimization, we note that other directions—considering different aspects of bone—exist for generating such structures. One such direction is material reconstruction. For instance, Liu and Shapiro [30] proposed to reconstruct 3D micro-structures from 2D sample images using example-based texture synthesis [31], such that the synthesized structures preserve statistical features of the given sample.

Another direction is the simulation of bone tissue adaptation using biology-inspired models. For instance, Huiskes et al. [32] proposed a biological model following Wolff's bone re-modeling theory [1] to simulate the process of bone resorption and formation under given mechanical stimuli. Numerical modeling of bone adaptation has been performed in computational mechanics by applying two-scale simulations (e.g., [33], [34], [35]), which date back to the seminal work by Bendsøe and Kikuchi [6]. The two-scale approach combines a fine scale composed of predefined optimal micro-structures with a coarse scale that is guided by finite element analysis and topology optimization. Besides the challenge of obtaining continuous micro-structural details between neighbouring coarse cells, the resulting structures are typically regular repetitions of (a limited amount of types of) cells. In contrast to these approaches, which strictly separate local and global scales, we propose to control local details by embedding geometric constraints into a unified simulation and optimization scale. This is similar to the approach by Alexandersen et al. [21], yet our approach provides higher geometric flexibility in that the resulting structures vary smoothly across the entire domain and geometric features are not restricted to a set of prescribed cell types.

3 Infill Optimization

We start by formulating a discrete optimization problem to generate porous structures, then introduce relaxations to enable an efficient numerical solution of the problem, and finally summarize the proposed algorithm. A 2D example

is used to demonstrate and explain the consequences of our derived formulation for the resulting structures.

3.1 Discrete Formulation

Our formulation is based on a regular hexahedral discretization of the design domain Ω that is covered by a given shape. For each volumetric element (i.e., voxel) e in the discretized model, a boolean value $\rho_e \in \{0, 1\}$ is assigned to indicate a solid ($\rho_e = 1$) or an empty voxel ($\rho_e = 0$). This leads to a binary field ρ representing the material distribution in Ω.

We define $\overline{\rho}_e$ to quantify the (local) material distribution in a neighbourhood surrounding the voxel e. In particular, $\overline{\rho}_e$ measures the percentage of solid voxels over all voxels in a prescribed neighbourhood $\mathbb{N}_e$, i.e.,

$$\overline{\rho}_e = \frac{\sum_{i \in \mathbb{N}_e} \rho_i}{\sum_{i \in \mathbb{N}_e} 1}. \tag{1}$$

$\mathbb{N}_e$ is the set of all surrounding voxels with a centroid that is closer than a given influence radius R_e to the centroid of voxel e, i.e.,

$$\mathbb{N}_e = \{i \mid ||x_i - x_e||_2 \leq R_e\}, \tag{2}$$

where x_i and x_e are the centroids of the voxels. The positions and lengths are measured in units of voxels. A local volume percentage $\overline{\rho}_e = 0.0$ (resp. $\overline{\rho}_e = 1.0$) means that all voxels in the defined neighbourhood are empty (resp. solid), and a value between 0.0 and 1.0 means that both empty and solid voxels exist.

With ρ and $\overline{\rho}$ defined, the optimization problem is given as

$$\min_{\rho} \quad c = \frac{1}{2} u^T K u, \tag{3}$$

$$\text{s.t.} \quad Ku = f, \tag{4}$$

$$\rho_e \in \{0, 1\}, \ \forall e, \tag{5}$$

$$\overline{\rho}_e \leq \alpha, \ \forall e. \tag{6}$$

The objective is to minimize the compliance, measured by the strain energy c, with u and K being the displacement vector and stiffness matrix, respctively. The displacement vector u is obtained by solving the static elasticity equation Eq. 4 under the external force vector f. Eq. 5 restricts the design variables to take discrete values 0 (empty) or 1 (solid).

The novel part in our formulation is Eq. 6. This constraint restricts the local material accumulation. For instance, $\alpha = 0.6$ implies that at most 60% of all voxels in $\mathbb{N}_e$ are solid while the other 40% are empty. Note that while this constraint restricts the percentage of the solid/empty voxels, it does not prescribe which specific voxels are solid or empty: Determining the specific solid and empty voxels is left to the optimizer, under the goal of minimizing the objective function. The rational behind this constraint is that it prevents material from being accumulated to form large solid regions, and as a consequence, the material will be distributed more evenly over the domain. This is in line with what we observe in nature when looking at porous structures such as trabecular bone.

We note that additional constraints such as a maximum total volume known from classical topology optimization can be integrated into this formulation as well. Its influence on the resulting structures, as well as the influence of other parameters will be discussed in Section 4.

3.2 Relaxations

The optimization problem given in Eq. 3-6 is a discrete optimization problem, with several millions of variables (cf. per-voxel design variable in Eq. 5) and constraints (cf. per-voxel constraint in Eq. 6) in some of our test cases. In the following, we present a number of relaxations to make the numerical optimization tractable.

3.2.1 *Constraint Aggregation*

The per-voxel local volume constraint (Eq. 6) gives rise to a large number of constraints. These constraints are equivalent to $\max_{\forall e}(\overline{\rho}_e) \leq \alpha$, which reduces the large number of constraints into a single constraint. However, it is not differentiable and, thus, not directly applicable to numerical optimization schemes. To overcome this problem, we use the p-norm function to approximate the $\max$ function,

$$\max_{\forall e}(\overline{\rho}_e) \approx ||\overline{\rho}||_p = (\sum_e \overline{\rho}_e^p)^{\frac{1}{p}}. \tag{7}$$

As p goes to infinite, $||\overline{\rho}||_p$ becomes equivalent to $\max_{\forall e}(\rho_e)$. To account for the difference between $\max_{\forall e}(\overline{\rho}_e)$ and $||\overline{\rho}||_p$ when the value of p is not infinitely large, we write the consolidated constraint $\max_{\forall e}(\overline{\rho}_e) \leq \alpha$ by

$$(\sum_e \overline{\rho}_e^p)^{\frac{1}{p}} \leq (\sum_e \alpha^p)^{\frac{1}{p}}, \tag{8}$$

which can be rearranged to

$$(\frac{1}{n} \sum_e \overline{\rho}_e^p)^{\frac{1}{p}} \leq \alpha, \tag{9}$$

where n is the number of elements. A larger p more strictly enforces the per-voxel constraints while increasing the non-linearity of the problem. In our examples we choose $p = 16$.

3.2.2 *Continuous Design Variable, Filtering, and Projection*

The discrete design variable (Eq. 5) necessitates expensive integer programming. To facilitate efficient gradient-based numerical optimization, we follow the study in [36] and introduce a per-voxel design variable ϕ_e which is allowed to take a scalar value continuously varying between 0.0 and 1.0,

$$\phi_e \in [0.0, \ 1.0]. \tag{10}$$

The field of design variables ϕ is first smoothed via a local convolution filter, and the filtered field $\tilde{\phi}$ is projected to obtain the material distribution ρ.

Filtering $\phi \rightarrow \tilde{\phi}$ The purpose of the filtering $\phi \rightarrow \tilde{\phi}$ is to remove checkerboard patterns (i.e., regions of alternating solid and void voxels) resulting from numerical instabilities [37]. In particular, the local filter calculates a weighted average of the neighbouring values via

$$\tilde{\phi}_e = \frac{\sum_{i \in \mathbb{M}_e} \omega_{i,e} \phi_i}{\sum_{i \in \mathbb{M}_e} \omega_{i,e}}. \tag{11}$$

Here, $\mathbb{M}_e$ is the set of voxels close to voxel e, i.e.,

$$\mathbb{M}_e = \{i \mid ||x_i - x_e||_2 \leq r_e\}, \tag{12}$$

with filter radius r_e. This filter size is different and smaller than the radius R_e in Eq. 2. The weighting factor $\omega_{i,e}$ depends linearly on the distance between the considered voxels, i.e.,

$$\omega_{i,e} = 1 - \frac{||x_i - x_e||_2}{r_e}. \tag{13}$$

Projection $\tilde{\phi} \to \rho$ The purpose of the projection $\tilde{\phi} \to \rho$ is to ensure a 0-1 solution. An intermediate value between 0.0 and 1.0 is thresholded at the value of $\frac{1}{2}$ to a discrete 0/1 value by

$$\rho_e(\tilde{\phi}_e) = \begin{cases} 1 & \text{if } \tilde{\phi}_e \geq \frac{1}{2}, \\ 0 & \text{otherwise.} \end{cases} \tag{14}$$

For numerical optimization, we relax ρ_e to a scalar threshold function and approximate this non-differential function by

$$\rho_e(\tilde{\phi}_e) = \frac{\tanh(\frac{\beta}{2}) + \tanh(\beta(\tilde{\phi}_e - \frac{1}{2}))}{2\ \tanh(\frac{\beta}{2})}. \tag{15}$$

The parameter β controls the sharpness of the threshold function, as illustrated in Fig. 2. An infinite β leads to a strict binary classification as in Eq. 14. Instead of directly applying a large β value, which results in highly non-linear equations, we start with $\beta = 1$ and double its value after a certain number of iterations. This process is known as parameter continuation, which is a common technique for improving convergence behaviour [36].

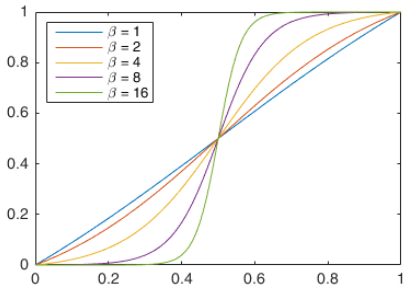

Fig. 2: The projection function Eq. 15 for various β values. As β increases, the function approaches the discrete function Eq. 14.

Material Interpolation With ρ_e being relaxed via Eq. 15 to a scalar, the Young's modulus corresponding to a voxel with continuous material distribution ρ_e is interpolated by

$$E_e(\rho_e) = E_{min} + \rho_e^{\gamma}\,(E_0 - E_{min}). \tag{16}$$

Here E_0 is the stiffness of the solid voxels, E_{min} is a very small stiffness assigned to empty voxels in order to prevent the global stiffness matrix from becoming singular, and γ is a penalization factor (typically $\gamma = 3$). Assuming a fixed Poisson's ratio the stiffness matrix of intermediate voxels then becomes

$$K_e = E_e(\rho_e)k_0, , \tag{17}$$

where k_0 is the element stiffness matrix for a voxel with unit Young's modulus. This interpolation scheme is known as modified Solid Isotropic Material Penalization (SIMP) [38].

3.3 Relaxed Formulation

With the above relaxations the optimization problem becomes

$$\min_{\phi} \quad c = \frac{1}{2}u^T K u, \tag{18}$$

$$\text{s.t.} \quad Ku = f, \tag{19}$$

$$\phi_e \in [0.0,\ 1.0],\ \forall e, \tag{20}$$

$$g(\phi) = \frac{(\frac{1}{n}\sum_e \overline{\rho}_e^{\,p})^{\frac{1}{p}}}{\alpha} - 1.0 \leq 0.0. \tag{21}$$

Here, the design variable is the continuous variable ϕ. This continuous optimization problem is solved iteratively by using gradient-based optimization schemes. In each iteration, three major steps are performed sequentially:

1) solve the state equation $Ku = f$ for the unknown displacement vector u,
2) do sensitivity analysis to get the derivatives of the objective and the constraint function with respect to the design variable ϕ, i.e., $\frac{\partial c}{\partial \phi}$ and $\frac{\partial g}{\partial \phi}$, and
3) update the design variables by a numerical optimization solver.

These three steps continue until the change of design variables in successive iterations falls below a prescribed threshold ϵ, or the number of iterations exceeds a maximum value $It_{\max}$. For the numerical optimization solver in step 3) we use the method of moving asymptotes (MMA) [39], [40].

Algorithm 1 details the optimization process. It takes as input the prescribed local volume fraction α and outputs the density field ρ representing the material distribution.

Algorithm 1 Infill optimization

Input: Local volume fraction α
Output: Density field ρ

Design variable $\phi = \alpha$
Iteration index $i = 0$
Design change $\Delta = 1.0$
Projection parameter $\beta = 1.0$
while $\Delta > \epsilon$ and $i \leq It_{\max}$ **do**
  $i = i + 1$
  $\tilde{\phi} \leftarrow \phi$ via Eq. 11
  $\rho \leftarrow \tilde{\phi}$ via Eq. 15
  $K \leftarrow \rho$ via Eq. 16 & 17
  u via solving $Ku = f$
  $c \leftarrow (u, K)$ via Eq. 18
  $\overline{\rho} \leftarrow \rho$ via Eq. 1
  $g \leftarrow (\overline{\rho}, \alpha)$ via Eq. 21
  $\frac{\partial c}{\partial \phi}$ & $\frac{\partial g}{\partial \phi}$ as in Appendix
  $\phi \leftarrow \left(c, g, \frac{\partial c}{\partial \phi}, \frac{\partial g}{\partial \phi}\right)$ via the MMA solver [40]
  $\Delta = \max_{\forall e}(|\phi_e^i - \phi_e^{i-1}|)$
  if $\mathrm{mod}(i, 40) == 0$ or $\Delta < \epsilon$ **then**
    $\beta = 2\beta$
    $\Delta = 1.0$
  end if
end while
Compute $\phi \to \tilde{\phi} \to \rho$

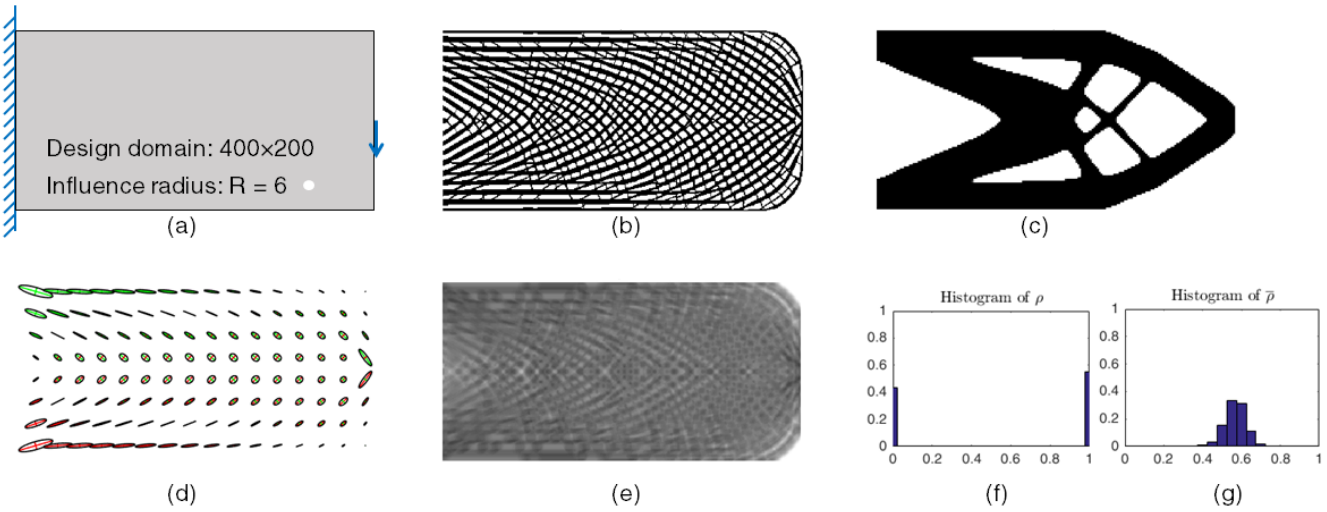

Fig. 3: (a) Illustration of the design domain, boundary conditions, and the local volume measurement region indicated by the size of the white disk. (b) Structure optimized by the proposed topology optimization with local volume constraints, i.e., the scalar field ρ. (c) Structure optimized by classical topology optimization with a total volume constraint. The compliance of (b) and (c) is 76.86 and 57.13, respectively, meaning that the structure considering local volume constraints is somewhat less stiff. (d) Visualization of the stress tensor field in the initial solid design domain. (e) The scalar local volume fraction $\overline{\rho}$. The grey scale is linearly mapped from the volume fraction. (f) The histogram of the obtained material distribution ρ. The values converge to a 0-1 solution. (g) The histogram of the local volume fraction $\overline{\rho}$. Most values fall below the prescribed local volume limit of 0.6.

3.4 Example

To demonstrate the effects of the proposed changes to classical topology optimization, a simple 2D example is used in the following. Fig. 3 (a) shows a rectangular 2D design domain. The left edge of the design domain is fixed, meaning that the displacements of the vertices along this edge are constrained to zero. On the right edge an external force is applied to the mid point. The design domain is discretized using a 400×200 uniform grid. A local volume fraction of $\alpha = 0.6$ and an influence radius of $R = 6$ are prescribed.

Fig. 3 (b) shows the optimized structure, where black and white indicate solid and empty elements, respectively. The structure has several distinctive features. First, compared to classical topology optimization with a prescribed volume constraint (Fig. 3 (c)), the material distribution does not evolve towards large solid and empty parts. The reason is that in the proposed formulation at most 60% of all voxels in each local neighbourhood are set to the solid state.

Second, the structure is dominated by crossing elongated sub-structures. As shown in Fig. 3 (d), where the stress tensor field in the initially solid design domain is visualized via ellipsoidal glyphs, the sub-structures largely follow the principal stress directions. The axes of the ellipses encode the principal stress directions and magnitudes at every voxel center. In addition, the colour of the axes indicate compression (red) or tension (green). While crossing sub-structures appear almost everywhere in the domain, single separated elongated structures can be found at the top and bottom of the left boundary. In theses regions the stresses are highly anisotropic (Fig. 3 (d)), and the material distribution has evolved primarily along the largest principal stress direction.

Third, the material is distributed across the entire design domain. This results from the objective to minimize compliance. If the constraint on material volume is not enforced, the minimization of compliance leads to a completely filled solid. Since local volume constraints are imposed, the optimizer tends to place material at every location up to the maximum allowed volume (60% in this case). The local volume values $\overline{\rho}$ are shown in Fig. 3 (e), and the histogram showing the frequency of occurrence of values is given in Fig. 3 (g). It can be seen that the majority of local volume values is below the prescribed limit of 0.6. At a few places, however, the prescribed local volume limit is exceeded, because the p-norm approximation does not represent the $\max$ function accurately. These values are mostly located in regions where the stress is very high.

The local volume constraint is parametrized by two values, the local volume limit α and the influence radius R. The effect of both parameters on the optimized structure is examined in Fig. 4. It can be seen that the local volume limit controls the local porosity, while the influence radius controls the empty space between substructures. As the influence radius increases, the locality constraint becomes less strict, leading to stiffer structures. If the influence radius becomes larger than the size of the design domain, the local volume constraints become equivalent to a total volume constraint, resulting in the stiffest structure as it would be generated by classical topology optimization.

4 Extensions

To provide further control over the optimized structures, we present several extensions to the infill optimization using Eq. 18-21 (referred to as the basic formulation in the

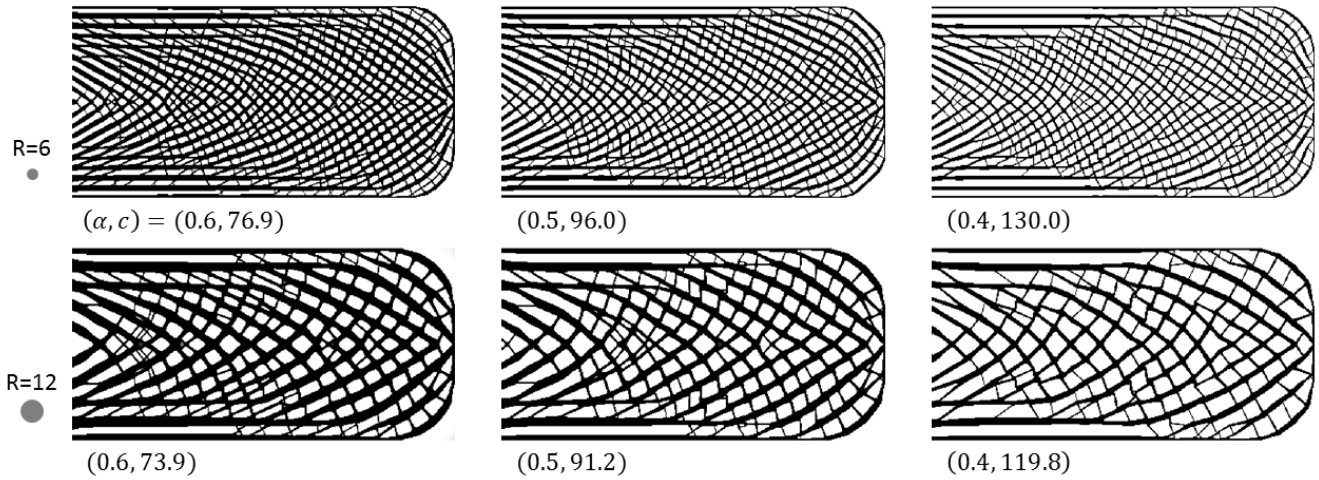

Fig. 4: From left to right, the local volume limit α deceases from 0.6 to 0.4. This leads to increasing porosity and a natural increase in the compliance value thereof. Structures in the bottom row were generated using a larger influence radius R, resulting in a less strict locality constraint and increasing stiffness of the structures thereof. In all examples, the same boundary conditions as illustrated in Fig. 3 (a) were applied.

following). The resulting infill structures are then compared to those resulting from the basic formulation.

4.1 Total Volume Control

By prescribing a maximum value for the total material volume, the user can control the expected cost of a print. Representing the voxel volume by v_e, which is constant in the regular discretization, the solid volume normalized by the volume of the design domain is

$$\rho_{avg} = \frac{\sum\limits_e \rho_e v_e}{\sum\limits_e v_e}. \tag{22}$$

The local volume constraint g (Eq. 21) implicitly imposes an upper bound on the total volume. In fact, the local upper bound α is a good indicator for the ratio of total volume ρ_{avg}, i.e., if $\rho_e = \alpha, \forall e$, we get $\rho_{avg} = \alpha$. However, since the density values ρ_e are set to either 0 or 1, and due to the domain boundaries, the resulting ρ_{avg} is smaller than α. For instance, $\rho_{avg} = 0.56$ when setting $\alpha = 0.6$ in the 2D test example.

To support direct control over the total volume, we integrate the following total volume constraint into the optimization problem:

$$g_1 = \rho_{avg} - \alpha_{total} \leq 0.0, \tag{23}$$

where α_{total} is a user-selected limit on the total volume ratio. The integration of this constraint into Algorithm 1 is straightforward. The constraint value g_1 and the value of its derivative $\frac{\partial g_1}{\partial \phi}$ are calculated and fed into the optimizer, together with their counterparts controlling the local volume, i.e., g and $\frac{\partial g}{\partial \phi}$.

Fig. 5 shows the result when different limits on the total material volume are used for optimizing the infill of the test shape in Fig. 3 (a). In all cases a local volume limit $\alpha = 0.6$ is imposed. In Fig. 5 (middle), as the total volume is controlled, structures disappear in regions of lower stresses (cf. the stress visualization in Fig. 3 (d)). In Fig. 5 (right), as the total volume is further reduced, the material distribution shrinks from low stress regions and evolves towards the structures that are generated by classical topology optimization (cf. Fig. 3 (c)).

4.2 Anisotropic Filter

In the basic formulation, we define the local volume fraction in a circular neighbourhood and treat all elements in this neighbourhood the same. However, since the stress distribution at some locations can be highly anisotropic, in such regions the material will accumulate along the major principal direction while leaving the other direction weakly or barely connected. This can be seen in the top and bottom left parts of the 2D object shown in Fig. 3-5. To further demonstrate the effect of anisotropy in the stress distribution, we show in Fig. 6 (a) a situation where the left edge of the cantilever is fixed, while uniformly distributed horizontal forces are applied to the right edge. Due to high uniaxial tension along the horizontal direction, the optimized structure is almost solely composed of horizontal bars (see Fig. 6 (b)).

To distribute the material along all directions, and thus to simulate natural bone remodelling, we suppress unidirectional growth by using anisotropic filters for defining the local volume fractions. Two and three such filters are used in 2D and 3D, respectively, with a 2D example shown in Fig. 7. Here, $90°$ degree orientations were used, yet other configurations can be used as well. For instance, one could use $60°$ oriented filters to obtain a higher degree of isotropy, or the filter axes could be oriented automatically along the principal stress direction determined by the finite element analysis of the initial shape. In 3D, the isotropic local volume measure $\overline{\rho}_e$ is substituted by three local volume measures corresponding to three different filter orientations,

$$\overline{\rho}_{e,s} = \frac{\sum_{i \in \mathbb{N}_{e,s}} \rho_i}{\sum_{i \in \mathbb{N}_{e,s}} 1}, \quad s \in \{x, y, z\}, \tag{24}$$

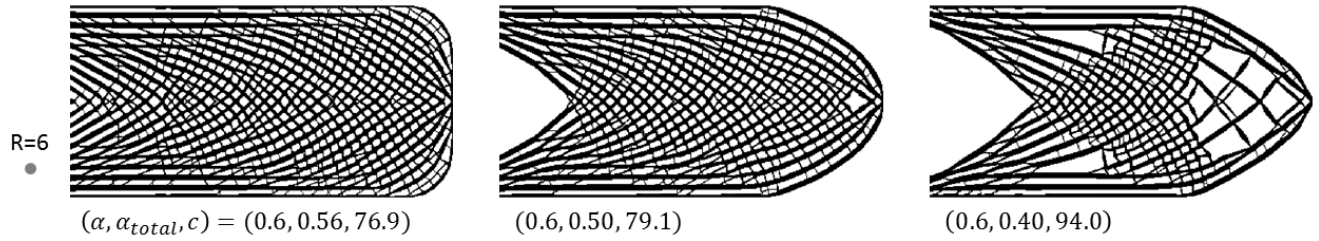

Fig. 5: In addition to a local volume limit of $\alpha = 0.6$, limits of $\alpha_{total} = 0.5$ (middle) and $\alpha_{total} = 0.4$ (right) were imposed on the global material distribution. The compliance increases due to the use of less material. The applied boundary conditions are shown in Fig. 3 (a).

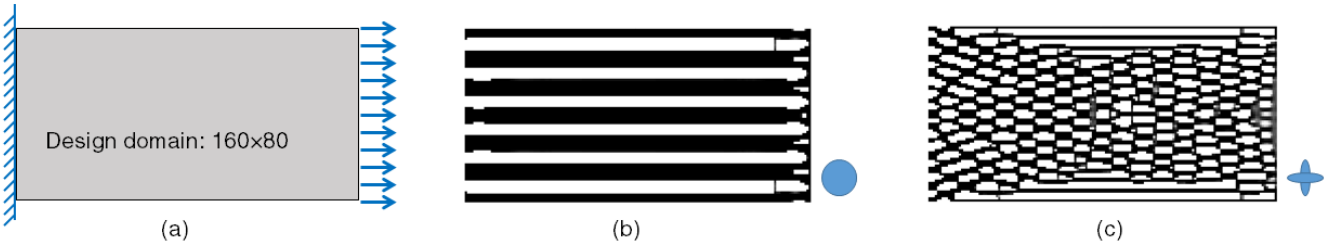

Fig. 6: Comparison of 2D structures optimized with isotropic and anisotropic filters. (a) Illustration of the design domain and boundary conditions. (b) The structure optimized with an isotropic filter, the size of which is indicated by the blue disk. (c) The structure optimized with anisotropic filters. The compliance and the total volume of (b) and (c) are 22.6 with 59.8% volume, and 34.6 with 51.7% volume, respectively.

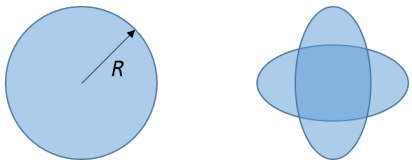

Fig. 7: Illustration of the influence region of a 2D isotropic filter (left) and two orthogonal anisotropic filters (right).

where $\mathbb{N}_{e,s}$ is the set of elements in the anisotropic influence region. Consequently, the constraint $\overline{\rho}_e \leq \alpha, \forall e$ is replaced by

$$\overline{\rho}_{e,s} \leq \alpha, \forall e, s \in \{x, y, z\}. \tag{25}$$

Fig. 6 (c) shows the result when the structure in (a) is optimized using two anisotropic filters. It can be seen that the horizontal bar-like structures are broken up, and instead the optimization process tries to connect short horizontal and vertical sub-structures.

In Fig. 8, the effects that can be achieved by using anisotropic filters in 3D are demonstrated. When the isotropic filter is used (top row), only a few connections along the y-axis evolve due to larger stresses in the xz-plane compared to those along the y-axis. When anisotropic filters are used (bottom row), more bridge-like connections between the planes parallel to the xz-plane are formed.

4.3 Truss- vs. Wall-like Structures

The local volume constraint suppresses the emergence of large solid domains. The two types of sub-structures that emerge primarily from this constraint are thin walls and trusses. A mix of both types evolves when optimizing 3D shapes (see Fig. 1). In the following, we discuss the parameters used to control the type of sub-structures and propose reformulations to prioritize or suppress certain types.

It has been shown recently [41] that thin-walls are the most effective 3D structures for stiffness optimization, as opposed to truss-like structures. Nevertheless, truss-like structures do appear very often in structural optimization, primarily due to an insufficient resolution of the underlying simulation grids. The spatial discretization implicitly requires the walls, if they exist, not to be thinner than one simulation element (and more if filtered). If the local material allowance is not sufficient for creating wall-like structures, holes are formed in the (not yet developed) walls. Given a higher resolution discretization, wall-like structures connecting the truss-like structures from a low spatial discretization emerge.

While from the perspective of solid mechanics closed-walled structures are more optimal, truss-like structures are found to dominate in trabecular bone. This can be attributed to the involved biofluid mechanics [42], i.e., truss-like structures allow unblocked interaction between the solid structures and the surrounding fluid environment. Truss-like structures are also preferable for their superior manufacturability, i.e., reducing the possibility of trapped powders in the post-processing of printed models. Since wall-like structures below the minimum feature size will fall apart into truss-like structures, the idea is to prescribe a larger minimum feature size (or alternatively a smaller maximum local volume) and, thus, to explicitly enforce the breakdown of closed-walled structures. The minimal feature size can be controlled by the filter radius r in the projection $\phi \rightarrow \tilde{\phi}$ [27], [36].

Fig. 9 compares the structures that were optimized with

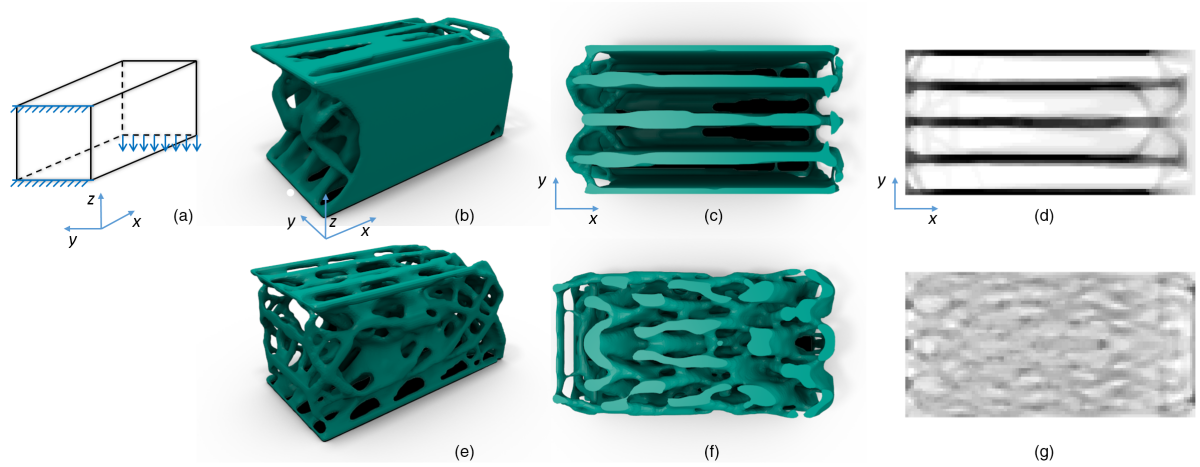

Fig. 8: Comparison of 3D structures optimized with isotropic and anisotropic filters. (a) Illustration of the design domain and boundary conditions. (b) The structure optimized with an isotropic filter. (c) The structure in (b) viewed from top, with a cut-plane parallel to the xy-plane. (d) The 3D density field is projected onto a 2D xy-plane, visualizing the distribution of averaged densities along rays parallel to the z-axis. (e,f,g) The structure optimized with anisotropic filters. The compliance and total volume resulting from isotropic and anisotropic filters are 79.4 with 27.9% volume, and 125.6 with 23.8% volume, respectively.

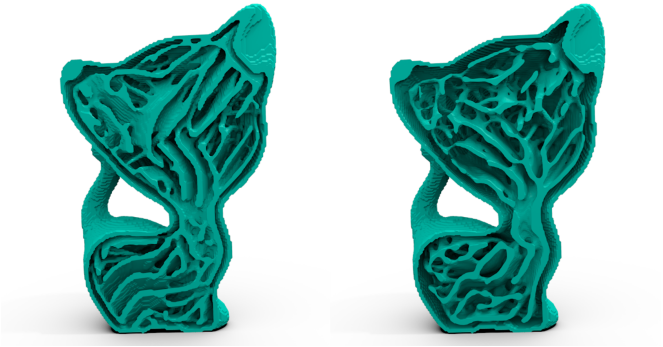

Fig. 9: As the minimum thickness increases from left to right, the wall-like structures are more and more replaced by truss-like structures.

different minimal feature sizes of $r = 2$ (left) and $r = 3$ (right). It can be seen that with increasing feature size some walls are substituted by a sparse set of trusses. Along with the breakdown of closed-walled structures, we observe a decrease of stiffness by a factor of up to 20%.

The relation between the minimal feature size and the structural types can be derived analytically. Consider a location x_e in the design domain. The influence region of an isotropic filter with radius R has a volume of $V_{sphere} = \frac{4}{3}\pi R^3$. A wall with a thickness of $2r$ takes a volume of $V_{wall} = 2\pi r R^2 - \frac{2}{3}\pi r^3$. To suppress the emergence of the wall, the allowed volume ratio α should be smaller than the required volume fraction, i.e.,

$$\alpha < \frac{V_{wall}}{V_{sphere}}. \tag{26}$$

This equation leads to the lower bound of the radius r under a prescribed volume allowance of α, and interchangeably, the upper bound of volume ratio α under a prescribed feature size r.

The above analysis is based on the assumption of strictly enforced local volume constraints, which is computationally prohibitive to realise. In our implementation, since we approximate the local volume constraints by a global p-norm, the actual volume fraction at locations where the stress is extremely high can be larger than the prescribed limit. Consequently, at such locations wall-like structures may still emerge.

4.4 Passive Elements

To fix a thin shell below the surface of a 3D input model, we prescribe elements close to the surface mesh as *passive* and denote the remaining elements as *active*. We compute a distance field in the design domain Ω to represent the shortest distance from the centroid of each element to the surface mesh. Elements with a distance below a prescribed layer thickness t are identified as passive. The thickness value can be adjusted by the user, and it was set to 2 times the voxel size in our experiments.

The local material distribution of passive elements is set to $\rho_e = 1.0$ and they are excluded from the design update step. Yet these solid elements are considered in the finite element analysis, since they can sustain forces as well. Passive elements are also excluded from the calculation of the local volume fraction for active elements. This is realised by augmenting the set of neighbouring elements, $\mathbb{N}_e$ in Eq. 2, by

$$\mathbb{N}_e = \{i \mid ||x_i - x_e||_2 \leq R_e, i \notin \Omega_s\}, \tag{27}$$

where e refers to an active element and Ω_s is the set of passive elements.

5 Results and Analysis

We have implemented the proposed infill optimization method in 2D based on the Matlab code provided in [38], and in 3D based on the high-performance multigrid solver

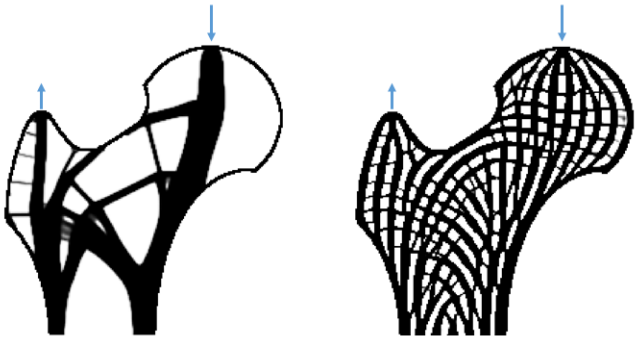

Fig. 10: Topology optimization in a 2D femur-shaped design domain. Left: Classical topology optimization with a total volume constraint. Right: Proposed topology optimization with local volume constraints.

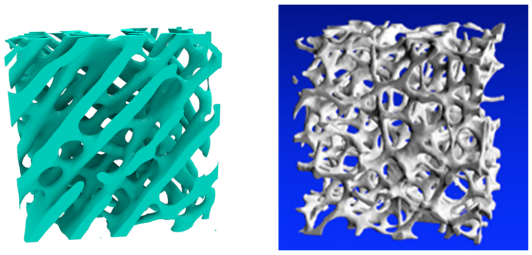

Fig. 11: Visual comparison of a cubic sample taken from the optimized infill in Fig. 1 and a real bone sample from CT scans (Image courtesy of R. Müller [45]).

for topology optimization proposed in [29]. In 3D, a surface mesh is constructed from the optimized scalar density field via the Marching Cubes algorithm [43] with a threshold value of $0.5^{\frac{1}{\gamma}}$, where γ is the penalization factor in material interoperation (Eq. 16) and takes a value of 3 in our examples. This mesh is smoothed via Taubin smoothing [44] with $\lambda = 0.5$ and $\mu = -0.53$ to eliminate staircase artifacts. In the following, we present and discuss a number of additional infills that have been generated by our method.

5.1 Bone Models

To verify that the proposed formulation leads to infills with a similar structure to trabecular bone, we prescribe a 2D femur-shaped design domain as shown in Fig. 10. The optimization is carried out with a total volume constraint (left) and local volume constraints (right). The porous infill on the right clearly follows the principal stress directions as depicted in Fig. 1.

As already indicated by Fig. 1, the 3D results are also very promising. The femur model is simulated with a resolution of $280 \times 185 \times 364$, leading to a total of 5.56 million finite elements. The femur model with the optimized infill was fabricated by using selective laser sintering using strong flexible plastic as printing material. The physical replica has a dimension of $12.32\,cm \times 5.85\,cm \times 16.00\,cm$.

Fig. 11 compares cubic samples taken from the optimized infill (left) and from a human femur CT scans (right). It can be seen that both samples are composed of sparse trusses and a few wall-like structures.

5.2 Robustness

With respect to material deficiency An advantage of distributed porous structures is their damage tolerance, i.e., the infill remains stiff even if parts are broken. Local failure can be caused by a high internal stress or by an accidental event. Stress-constrained topology optimization is formed to prevent stress-induced failure. Here we examine the structural integrity when local failure happens, for instance, due to collision, explosion, corrosion, fatigue failure, and manufacturing error. In particular, we employ a simplified local damage model [46] and assume that a quadrilateral region of a fixed size is damaged, and that this region can be placed anywhere in the design domain. It is desired that in case of damage a high stiffness can be maintained.

We test the damage tolerance of different structures generated for the half MBB-beam at a grid resolution of 200×100 (see Fig. 12). We first optimize with respect to local volume constraints using a local volume limit of $\alpha = 0.4$ (middle). The influence radius is selected based on the assumed damage size, effectively controlling the amount of empty space between porous structures. The resulting volume ($\alpha_{total} = 0.368$) is then considered in a second optimization with respect to the total volume constraint (left). A regular grid (right) with the same volume serves as a reference. To exactly match the prescribed volume, the thickness of the horizontal bars is slightly enhanced at the bottom.

To simulate damage, we remove the material in a certain region—indicated by the orange squares in Fig. 12—from the optimized structures. The damaged shapes are then compared with respect to their compliance. While the total volume constrained infill (left) has a compliance of 101.4 before and 1763.8 after damage, the local volume constrained infill (middle) has a compliance of 132.6 before and 187.3 after damage. This suggests that the infill that was optimized with respect to the total volume is very sensitive to material damages – The compliance changes by a factor of 17.4, while it changes only by a factor of 1.4 for the porous infill.

To consider the sensitivity of the structural compliance to the applied damage, we vertically move the damage region downwards and consecutively evaluate the compliance. The curves in Fig. 13 show the resulting changes for all three test structures. It can be seen that the bone-like infill (green curve) exhibits only small variations in the compliance values. The total volume constrained structure undergoes large changes under some damage conditions. For the regular infill, even though it also shows only minor variations, the compliance values are about 4 times larger than those of the bone-like infill.

With respect to force variations The second benefit of porous structures is their robustness with respect to force variations as they often occur in practical use cases. To demonstrate this, we evaluate the robustness of the 2D bone model to varying force conditions (see Fig. 14). The structures are optimized with respect to the forces indicated by the dashed grey arrows, under a total volume constraint (left) and the local volume constraints (middle). We then rotate the forces by $\frac{\pi}{4}$ as represented by the solid blue arrows and re-calculate the compliance of the structures

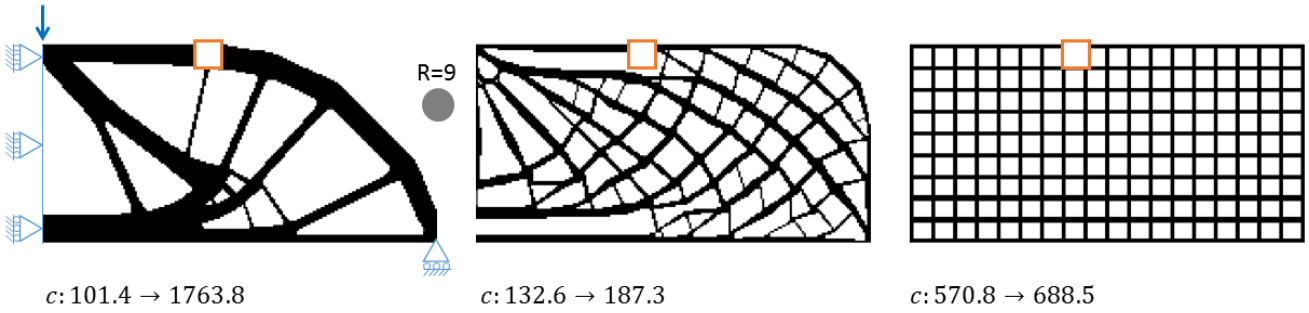

Fig. 12: Illustration of local material damage. Without damage, the structure constrained to a total volume (left) has the smallest compliance c of the three structures. When damaged as indicated by the orange square, this structure's compliance becomes worst. The middle structure was generated by constraining the local volume limit. A regular grid structure (right) serves as reference.

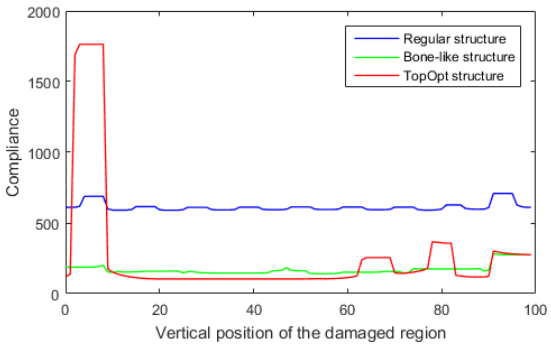

Fig. 13: Change in compliance with respect to a constantly relocated damage region for the three designs in Fig. 12. The bone-like porous infill (green) has a smaller variation and a small worst-case compliance.

under the new force condition. The total volume constrained infill is very sensitive to this change of direction, i.e., the compliance changes from 30.54 to 45.83. In contrast, the compliance of the local volume constrained version changes only from 36.72 to 36.23.

To examine the sensitivity of the compliance to varying force directions, we consecutively rotate the force directions out of an initial start configuration. Fig. 15 shows the compliance values depending on the rotation of force direction. The regular infill (blue, top) and the fully solid infill (cyan, bottom) serve as references. At an angle of attack of zero degrees, for which the structures were optimized, both the total volume (red) and local volume (green) constrained structures have a compliance close to that of the solid structure, with the total volume constrained structure performing slightly better. At angles up to about $20°$ the red curve remains below the green one, indicating a somewhat higher stiffness of the total volume constrained structure. Beyond $20°$ the red curve exceeds the green one, indicating the superiority of the local volume constrained structure as well as the sensitivity of the total volume constrained structure to large directional changes. At the rotation angle of $90°$, both structures show their worst-case compliance.

Our test verifies the robustness of the local volume constrained structure, which is in agreement with the formation of porous structures in bone. The mechanical load applied to a bone is not static but varies during day-to-day work. Thus, a bone permanently undergoes a dynamic natural optimization process and produces porous structures accounting for all different load conditions.

5.3 Convergence & Performance

Convergence Fig. 16 provides insights into the convergence of the numerical optimization scheme applied to the 2D cantilever model. Along the horizontal axis we indicate the number of iterations. The vertical axis represents from left to right the compliance value, i.e., the objective in Eq. 18, the constraint in Eq. 21, and the sharpness

$$s = \frac{4}{n}\sum_e(\rho_e(1-\rho_e)), \tag{28}$$

to measure how close the continuous density field is to a binary field [47]. Here n is the number of elements. On the right and from top to bottom, three structures corresponding to the density field at iterations 79, 159, and 279 are shown.

It can be observed that the compliance gradually decreases during the optimization process, indicating increasing stiffness of the structure. The constraint value is maintained below 0.0, while a few jumps happen when the β value is doubled every 40-th iteration. This β-continuation is required to convert the intermediate values into a strict 0-1 solution cf. earlier discretization. When the density values are converged to a strict 0-1 solution the sharpness factor becomes 0.0, and it becomes 1.0 if all elements take a value of 0.5. The structures on the right indicate that the design becomes more and more discrete with progressing optimization. Even though the optimization can be stopped before converging to a discrete design, which is common practice when using classical topology optimization in industry, this bears the risk of computing a misinterpreted topology.

Performance Table 1 reports on the complexity of the used 3D simulation models and gives timing statistics for different parts of the optimization process under local volume constraints. All experiments were run on a standard desktop PC equipped with an Intel Xeon E5-1650 v3 processor (12 cores) running at 3.50 GHz, 32 GB of RAM, and an NVIDIA GTX1080 graphics card with 8 GB memory. We

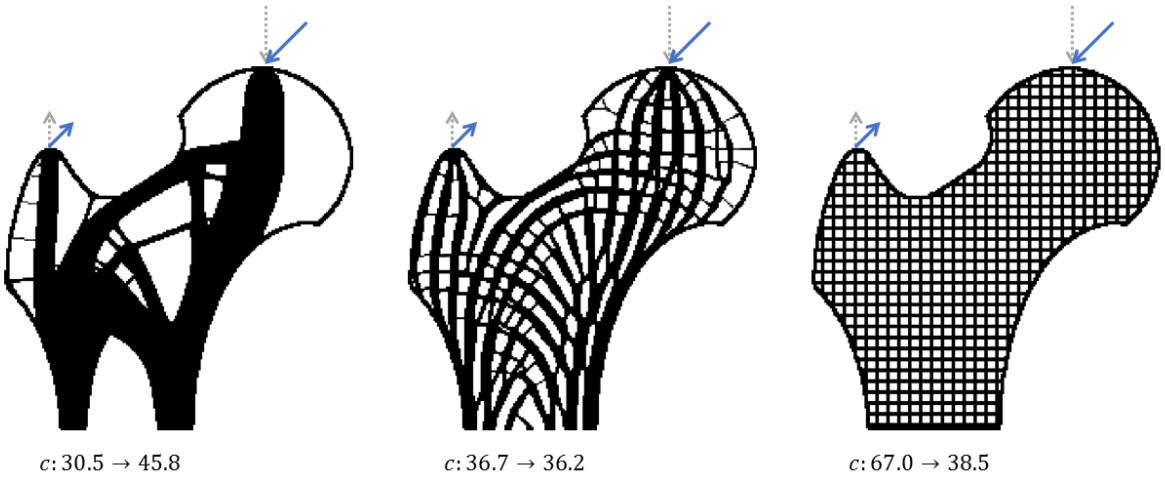

Fig. 14: The structures are optimized with respect to the force condition as indicated by the dashed grey arrows. Under alternative forces (solid blue arrows), the local volume constrained structure (middle) is 1.3 times stiffer than the total volume constrained structure (left). The regular grid with the same amount of volume on the right serves as a reference.

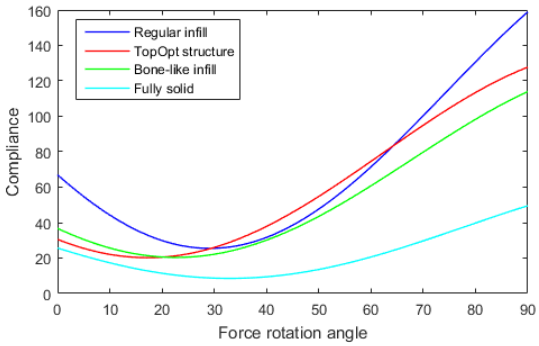

Fig. 15: The compliance with respect to changing force directions for the 2D femur model (Fig. 14). The bone-like porous infill (green) is less sensitive to changes in the force direction and has a smaller worst-case compliance compared to the total volume constrained structure (red).

Model	Resolution	# Ele.	Per iteration [s]			# Iter.	Total [min]
			FEM	Sens.	MMA		
Femur	280×185×364	5.6e6	6.85	5.44	2.52	500	121.2
Kitten	218×198×334	4.6e6	5.45	4.54	1.91	120	23.8
Cantilever	200×100×100	2.0e6	1.98	2.11	0.95	120	10.1

TABLE 1: Performance statistics for different models.

break down the computing time into three parts: FEM, sensitivity analysis including data preparation for MMA, and MMA. The computations involved in all stages consist predominantly of matrix and vector operations, and they are thus highly parallelizable. The FEM analysis, which turns out to be the performance bottleneck, is accelerated via a highly efficient geometric multigrid solver and GPU parallelization [29]. The multigrid solver is terminated at a residual reduction of 10^{-4}. For the sensitivity analysis, we execute the convolution operator with a larger R on the GPU. All other matrix operations as well as the MMA solver are parallelized with OpenMP [40]. The design optimization is performed iteratively using a fixed number of iterations.

5.4 Comparison

Comparison to honeycomb structures Fig. 17 compares the compliance-minimized structures subject to local and global volume constraints to the volume-minimized honeycomb structure subject to a critical stress [12]. The three models are optimized with the same material properties and boundary conditions. From the stress distribution (left) it can be observed that the forces applied at the top of the kitten model are transmitted mostly through the neck and the tail to the fixed bottom part. This results in a straight structure connecting the top and the bottom when using classical topology optimization (middle). Since in the new formulation the local volume is controlled, the vertical structure splits into multiple curved structures (right). The compliance values are normalized against the compliance of a fully solid shape. The values indicate that the porous infill is 1.5 times stiffer than the honeycomb structure, and has a maximum von Mises stress that is 72.5% of the maximum stress in the honeycomb structure.

Comparison to rhombic structures In Fig. 18, we show a comparison to self-supporting rhombic infill structures [16]. This example employs the same boundary conditions as in Fig. 17, but it uses a larger volume percentage in order to allow the rhombic wall to be thicker than three voxels in a stable finite element analysis. The optimized rhombic infill (left) supports the forces by an adaptive refinement in the vertical region. The uniformly refined infill (middle) serves as a reference. The bone-like porous infill (right) exhibits a similar trend as in Fig. 17 (right). The porous infill is about 1.14 times stiffer than the optimized rhombic structure at comparable maximum stresses. Both optimized structures perform better than the uniform grid.

The measure on 3D structures optimized via both the conventional topology optimization and the proposed infill optimization is based on black-white designs, i.e., the solid shapes that are converted from the density fields by a threshold value of 0.79 (i.e., $0.5^{\frac{1}{\gamma}}$, with $\gamma = 3$). From experiments we find that the difference in compliances due to this conversion generally is small and at most 1%.

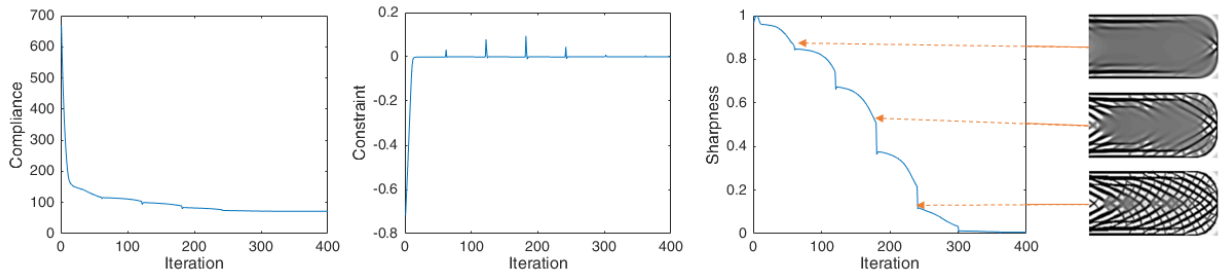

Fig. 16: Convergence plots of the compliance (left), the constraint (middle), and the sharpness of the density field (right) over the iterative optimization process. The density field, shown at three different stages on the right, gradually converges to a 0-1 solution by using β-continuation in Eq. 15. This explains the discontinuities at every 40-th iteration.

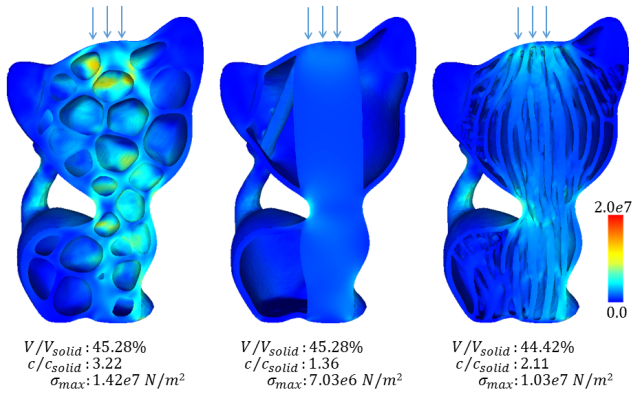

Fig. 17: Comparison between the honeycomb structure [12] (left, model courtesy of Lu et al.) and structures generated by topology optimization with a total volume constraint [29] (middle) and with local volume constraints (right).

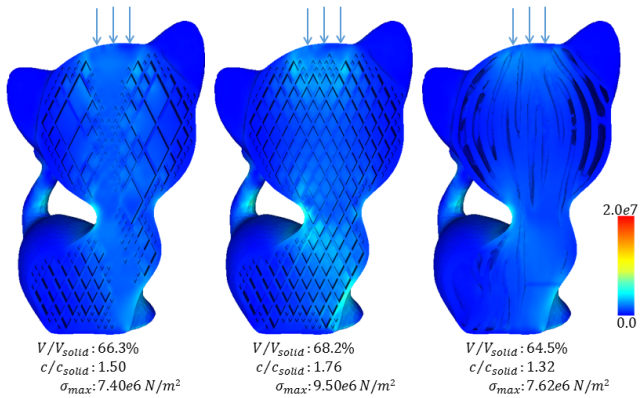

Fig. 18: Comparison between self-supporting rhombic infill structures [16] that are refined adaptively (left) and uniformly (middle), and the structure generated by local volume constrained topology optimization (right).

5.5 Discussion

Robustness We have tested bone-like infills under different robustness criteria. Natural materials seem to suggest that structural robustness comes with organized complexity in shape and topology [3]. The local volume constraint serves this purpose by encouraging a structural organization of micro-structures to support prescribed external forces. The very typical approach to ensure robustness to uncertain loads in topology optimization is to optimize with respect to multiple or worst case loading scenarios. This is a wide spread concept (c.f. [48], or some quite recent examples [49], [50], [51]). However, such approaches require some *a priori* knowledge of the positions of these uncertain loads; anti-optimization problems may have to be solved to identify worst cases; and many load cases (c.f. expensive finite element analyses) must be performed to ensure a reasonable coverage of the uncertainties. To achieve low sensitivity to loading positions and detailed structures as shown in our work, dozens (if not hundreds) of loads with varying location and direction would be necessary. In contrast, our formulation involves only one (or possibly a few) finite element analysis in each iteration. This makes the new formulation more practical for processing the massive models as we see in 3D printing.

Manufacturability While additive manufacturing enables the fabrication of complex shapes, it still poses a few constraints, e.g., regarding feature size, enclosed voids, and overhang surfaces. Ideally such constraints shall be incorporated into the optimization process. Otherwise a post-process might become necessary, and this process can counteract optimality. In our work we have taken into account the minimum feature size by the well-established projection method [27], [36]. Concerning the enclosed voids which might trap unsintered powder in SLS (Selective Laser Sintering), in Section 4.3 we have analyzed parameters which influence the formation of wall-like structures. Nevertheless, a rigorous formulation to guarantee enclosed-void-free is currently out of reach. Regarding overhang avoidance, some progress has been made recently by embedding corresponding constraints into density-based topology optimization [52], [53], [54]. These methods are compatible to our formulation, yet we leave the integration as future work.

To verify the manufacturability of bone-like infills, we have fabricated the femur model using the SLS process (see Fig. 1) and three additional models using more affordable FDM (Fused Deposition Modelling) printers (see Fig. 19). When using FDM printers, the models could be printed without supports for the infill, since, in general, the bone-like infills show small overhang areas that are within the allowed tolerance. The absence of supports leaves a few visual artefacts and unguaranteed mechanical property.

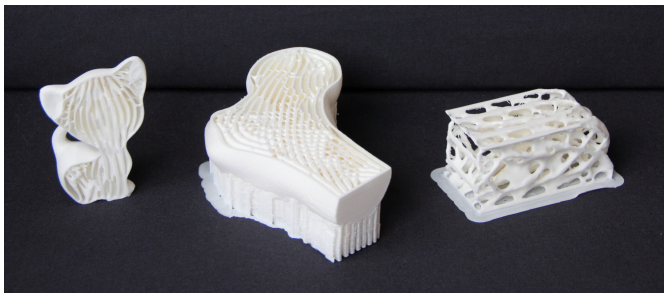

Fig. 19: FDM printed replicas of some models generated by our formulation.

6 Conclusion

We have presented a structural optimization method for obtaining stiffness optimized porous structures. These numerically optimized structures visually resemble trabecular bone, which is lightweight and robust with respect to material deficiency and force variations. This makes the optimized interior structures an ideal candidate for application-specific infill in additive manufacturing.

Appendix

In numerical optimization, the gradient of the objective c and the constraint g with respective to the design variable ϕ is needed. It is calculated using the chain rule as follows

$$\frac{\partial c}{\partial \phi_e} = \sum_{i \in \mathbb{M}_e} \left(\frac{\partial c}{\partial \rho_i} \frac{\partial \rho_i}{\partial \tilde{\phi}_i} \frac{\partial \tilde{\phi}_i}{\partial \phi_e} \right), \tag{29}$$

$$\frac{\partial g}{\partial \phi_e} = \sum_{i \in \mathbb{M}_e} \left(\sum_{j \in \mathbb{N}_i} \left(\frac{\partial g}{\partial \overline{\rho}_j} \frac{\partial \overline{\rho}_j}{\partial \rho_i} \right) \frac{\partial \rho_i}{\partial \tilde{\phi}_i} \frac{\partial \tilde{\phi}_i}{\partial \phi_e} \right). \tag{30}$$

The derivative $\frac{\partial c}{\partial \rho_i}$ is calculated using the adjoint analysis

$$\frac{\partial c}{\partial \rho_i} = -\gamma \rho_i^{\gamma-1} (E_0 - E_{\min}) u_i^{\mathrm{T}} k_0 u_i. \tag{31}$$

The other components can be derived as

$$\frac{\partial \rho_i}{\partial \tilde{\phi}_i} = \frac{\beta(1.0 - \tanh^2(\beta(\tilde{\phi}_i - \frac{1}{2})))}{2\tanh(\frac{\beta}{2})}, \tag{32}$$

$$\frac{\partial \tilde{\phi}_i}{\partial \phi_e} = \frac{\omega_{e,i}}{\sum\limits_{k \in \mathbb{M}_i} \omega_{k,i}}, \tag{33}$$

$$\frac{\partial g}{\partial \overline{\rho}_j} = \frac{1}{\alpha n} \left(\frac{1}{n} \sum_e \overline{\rho}_e^p \right)^{\frac{1}{p}-1} {\overline{\rho}_j}^{p-1}, \tag{34}$$

$$\frac{\partial \overline{\rho}_j}{\partial \rho_i} = \frac{1}{\sum\limits_{k \in \mathbb{N}_j} 1}. \tag{35}$$

Acknowledgements

The authors gratefully acknowledge the support from the H.C. Ørsted Postdoc Programme at the Technical University of Denmark, which has received funding from the People Programme (Marie Curie Actions) of the European Union's Seventh Framework Programme (FP7/2007-2013) under REA grant agreement no. 609405 (COFUNDPostdocDTU), and the support from the Villum foundation through the NextTop project.

References

[1] J. Wolff, "Das gesetz der transformation der knochen," *DMW-Deutsche Medizinische Wochenschrift*, vol. 19, no. 47, pp. 1222–1224, 1893.

[2] M. A. Meyers, P.-Y. Chen, A. Y.-M. Lin, and Y. Seki, "Biological materials: Structure and mechanical properties," *Progress in Materials Science*, vol. 53, no. 1, pp. 1 – 206, 2008.

[3] U. G. Wegst, H. Bai, E. Saiz, A. P. Tomsia, and R. O. Ritchie, "Bioinspired structural materials," *Nature materials*, vol. 14, no. 1, pp. 23–36, 2015.

[4] "Bone structure and function," https://depts.washington.edu/bonebio/ASBMRed/structure.html, accessed: 2016-04-18.

[5] C. Dick, J. Georgii, R. Burgkart, and R. Westermann, "Stress tensor field visualization for implant planning in orthopedics," *IEEE Trans. Vis. Comput. Graphics*, no. 6, pp. 1399–1406, 2009.

[6] M. P. Bendsøe and N. Kikuchi, "Generating optimal topologies in structural design using a homogenization method," *Comput Methods Appl Mech Eng*, vol. 71, no. 2, pp. 197–224, 1988.

[7] M. P. Bendsøe and O. Sigmund, *Topology optimization: theory, methods, and applications*. Springer-Verlag Berlin Heidelberg, 2004.

[8] W. Gao, Y. Zhang, D. Ramanujan, K. Ramani, Y. Chen, C. B. Williams, C. C. Wang, Y. C. Shin, S. Zhang, and P. D. Zavattieri, "The status, challenges, and future of additive manufacturing in engineering," *Computer-Aided Design*, vol. 69, pp. 65–89, 2015.

[9] L. Liu, A. Shamir, C. Wang, and E. Whiting, "3d printing oriented design: Geometry and optimization," in *SIGGRAPH Asia 2014 Courses*, 2014.

[10] J. Smith, J. Hodgins, I. Oppenheim, and A. Witkin, "Creating models of truss structures with optimization," *ACM Trans. Graph.*, vol. 21, no. 3, pp. 295–301, 2002.

[11] W. Wang, T. Y. Wang, Z. Yang, L. Liu, X. Tong, W. Tong, J. Deng, F. Chen, and X. Liu, "Cost-effective printing of 3d objects with skin-frame structures," *ACM Trans. Graph.*, vol. 32, no. 6, pp. 177:1–177:10, Nov. 2013.

[12] L. Lu, A. Sharf, H. Zhao, Y. Wei, Q. Fan, X. Chen, Y. Savoye, C. Tu, D. Cohen-Or, and B. Chen, "Build-to-last: Strength to weight 3D printed objects," *ACM Trans. Graph.*, vol. 33, no. 4, pp. 97:1–97:10, Jul. 2014.

[13] O. Stava, J. Vanek, B. Benes, N. Carr, and R. Měch, "Stress relief: Improving structural strength of 3d printable objects," *ACM Trans. Graph.*, vol. 31, no. 4, pp. 48:1–48:11, Jul. 2012.

[14] Q. Zhou, J. Panetta, and D. Zorin, "Worst-case structural analysis," *ACM Trans. Graph.*, vol. 32, no. 4, pp. 137:1–137:12, Jul. 2013.

[15] H. Zhao, F. Gu, Q.-X. Huang, J. Garcia, Y. Chen, C. Tu, B. Benes, H. Zhang, D. Cohen-Or, and B. Chen, "Connected fermat spirals for layered fabrication," *ACM Trans. Graph.*, vol. 35, no. 4, pp. 100:1–100:10, Jul. 2016.

[16] J. Wu, C. C. Wang, X. Zhang, and R. Westermann, "Self-supporting rhombic infill structures for additive manufacturing," *Computer-Aided Design*, vol. 80, pp. 32 – 42, 2016.

[17] C. Schumacher, B. Bickel, J. Rys, S. Marschner, C. Daraio, and M. Gross, "Microstructures to control elasticity in 3d printing," *ACM Trans. Graph.*, vol. 34, no. 4, pp. 136:1–136:13, Jul. 2015.

[18] J. Panetta, Q. Zhou, L. Malomo, N. Pietroni, P. Cignoni, and D. Zorin, "Elastic textures for additive fabrication," *ACM Trans. Graph.*, vol. 34, no. 4, pp. 135:1–135:12, Jul. 2015.

[19] J. Martínez, J. Dumas, and S. Lefebvre, "Procedural Voronoi foams for additive manufacturing," *ACM Trans. Graph.*, vol. 35, no. 4, pp. 44:1–44:12, Jul. 2016.

[20] E. Andreassen, B. S. Lazarov, and O. Sigmund, "Design of manufacturable 3d extremal elastic microstructure," *Mechanics of Materials*, vol. 69, no. 1, pp. 1 – 10, 2014.

[21] J. Alexandersen and B. S. Lazarov, "Topology optimisation of manufacturable microstructural details without length scale separation using a spectral coarse basis preconditioner," *Comput Methods Appl Mech Eng*, vol. 290, pp. 156 – 182, 2015.

[22] O. Sigmund and K. Maute, "Topology optimization approaches," *Struct. Multidiscip. Optim.*, vol. 48, no. 6, pp. 1031–1055, 2013.

[23] J. D. Deaton and R. V. Grandhi, "A survey of structural and multidisciplinary continuum topology optimization: post 2000," *Struct. Multidiscip. Optim.*, vol. 49, no. 1, pp. 1–38, 2014.

[24] O. Sigmund, "A 99 line topology optimization code written in Matlab," *Struct. Multidiscip. Optim.*, vol. 21, no. 2, pp. 120–127, Apr. 2001.

[25] T. A. Poulsen, "A new scheme for imposing a minimum length scale in topology optimization," *Int J Numer Meth Eng*, vol. 57, no. 6, pp. 741–760, 2003.
[26] B. S. Lazarov, F. Wang, and O. Sigmund, "Length scale and manufacturability in density-based topology optimization," *Archive of Applied Mechanics*, vol. 86, no. 1, pp. 189–218, 2016.
[27] J. K. Guest, J. Prévost, and T. Belytschko, "Achieving minimum length scale in topology optimization using nodal design variables and projection functions," *Int J Numer Meth Eng*, vol. 61, no. 2, pp. 238–254, 2004.
[28] J. Guest, "Imposing maximum length scale in topology optimization," *Struct. Multidiscip. Optim.*, vol. 37, no. 5, pp. 463–473, 2009.
[29] J. Wu, C. Dick, and R. Westermann, "A system for high-resolution topology optimization," *IEEE Trans. Vis. Comput. Graphics*, vol. 22, no. 3, pp. 1195–1208, March 2016.
[30] X. Liu and V. Shapiro, "Random heterogeneous materials via texture synthesis," *Computational Materials Science*, vol. 99, pp. 177 – 189, 2015.
[31] L.-Y. Wei, S. Lefebvre, V. Kwatra, and G. Turk, "State of the art in example-based texture synthesis," in *Eurographics 2009, State of the Art Report, EG-STAR*. Eurographics Association, 2009, pp. 93–117.
[32] R. Huiskes, R. Ruimerman, G. H. Van Lenthe, and J. D. Janssen, "Effects of mechanical forces on maintenance and adaptation of form in trabecular bone," *Nature*, vol. 405, no. 6787, pp. 704–706, 2000.
[33] P. Coelho, P. Fernandes, H. Rodrigues, J. Cardoso, and J. Guedes, "Numerical modeling of bone tissue adaptationa hierarchical approach for bone apparent density and trabecular structure," *Journal of Biomechanics*, vol. 42, no. 7, pp. 830 – 837, 2009.
[34] X. Wang, S. Xu, S. Zhou, W. Xu, M. Leary, P. Choong, M. Qian, M. Brandt, and Y. M. Xie, "Topological design and additive manufacturing of porous metals for bone scaffolds and orthopaedic implants: A review," *Biomaterials*, vol. 83, pp. 127 – 141, 2016.
[35] F. Schury, M. Stingl, and F. Wein, "Efficient two-scale optimization of manufacturable graded structures," *SIAM Journal on Scientific Computing*, vol. 34, no. 6, pp. B711–B733, 2012.
[36] F. Wang, B. S. Lazarov, and O. Sigmund, "On projection methods, convergence and robust formulations in topology optimization," *Struct. Multidiscip. Optim.*, vol. 43, no. 6, pp. 767–784, 2010.
[37] A. Díaz and O. Sigmund, "Checkerboard patterns in layout optimization," *Structural optimization*, vol. 10, no. 1, pp. 40–45, 1995.
[38] E. Andreassen, A. Clausen, M. Schevenels, B. S. Lazarov, and O. Sigmund, "Efficient topology optimization in Matlab using 88 lines of code," *Struct. Multidiscip. Optim.*, vol. 43, no. 1, pp. 1–16, 2010.
[39] K. Svanberg, "The method of moving asymptotes—a new method for structural optimization," *Int J Numer Meth Eng*, vol. 24, no. 2, pp. 359–373, 1987.
[40] N. Aage and B. S. Lazarov, "Parallel framework for topology optimization using the method of moving asymptotes," *Struct. Multidiscip. Optim.*, vol. 47, no. 4, pp. 493–505, 2013.
[41] O. Sigmund, N. Aage, and E. Andreassen, "On the (non-) optimality of Michell structures," *Struct. Multidiscip. Optim.*, pp. 1–13, 2016.
[42] E. Birmingham, J. A. Grogan, G. L. Niebur, L. M. McNamara, and P. E. McHugh, "Computational modelling of the mechanics of trabecular bone and marrow using fluid structure interaction techniques," *Annals of Biomedical Engineering*, vol. 41, no. 4, pp. 814–826, 2013.
[43] W. E. Lorensen and H. E. Cline, "Marching cubes: A high resolution 3d surface construction algorithm," in *SIGGRAPH '87*. New York, NY, USA: ACM, 1987, pp. 163–169.
[44] G. Taubin, "A signal processing approach to fair surface design," in *SIGGRAPH '95*. New York, NY, USA: ACM, 1995, pp. 351–358.
[45] R. Müller and P. Rüegsegger, "Micro-tomographic imaging for the nondestructive evaluation of trabecular bone architecture." *Studies in health technology and informatics*, vol. 40, pp. 61–79, 1997.
[46] M. Jansen, G. Lombaert, M. Schevenels, and O. Sigmund, "Topology optimization of fail-safe structures using a simplified local damage model," *Struct. Multidiscip. Optim.*, vol. 49, no. 4, pp. 657–666, 2014.
[47] O. Sigmund, "Morphology-based black and white filters for topology optimization," *Struct. Multidiscip. Optim.*, vol. 33, no. 4, pp. 401–424, 2007.
[48] M. P. Bendsøe, A. Ben-Tal, and J. Zowe, "Optimization methods for truss geometry and topology design," *Structural optimization*, vol. 7, no. 3, pp. 141–159, 1994.
[49] G. Allaire, F. de Gournay, and F. Jouve, "Stress minimization and robust compliance optimization of structures by the level set method," in *8th World Congress on Structural and Multidisciplinary Optimization*, 2009.
[50] M. Schevenels, B. Lazarov, and O. Sigmund, "Robust topology optimization accounting for spatially varying manufacturing errors," *Comput Methods Appl Mech Eng*, vol. 200, no. 4952, pp. 3613 – 3627, 2011.
[51] K. Cai, Z. Luo, and Y. Wang, *Topology Optimization for Human Proximal Femur Considering Bi-modulus Behavior of Cortical Bones*. Cham: Springer International Publishing, 2015, pp. 263–270.
[52] M. Langelaar, "An additive manufacturing filter for topology optimization of print-ready designs," *Struct. Multidiscip. Optim.*, pp. 1–13, 2016.
[53] A. T. Gaynor and J. K. Guest, "Topology optimization considering overhang constraints: Eliminating sacrificial support material in additive manufacturing through design," *Struct. Multidiscip. Optim.*, pp. 1–16, 2016.
[54] X. Qian, "Undercut and overhang angle control in topology optimization: a density gradient based integral approach," *Int J Numer Meth Eng*, pp. n/a–n/a, nme.5461.

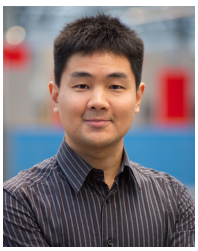

Jun Wu is a PostDoc at the Department of Mechanical Engineering at the Technical University of Denmark. He received a PhD in Computer Science in 2015 from the Technical University of Munich, Germany, and a PhD in Mechanical Engineering in 2012 from Beihang University, Beijing, China, where he also received a B.Eng in Astronautics Engineering in 2006. His research is focused on geometric and physical modeling, with applications in surgical simulation and design optimization.

Niels Aage is an Associate Professor at the Department of Mechanical Engineering at the Technical University of Denmark. He received his PhD in Optimal Design in 2011 from the Technical University of Denmark. His research interest is focused on the area of large scale, parallel numerical methods for PDE constrained optimization, with emphasis on topology and shape optimization problems in multiphysical settings.

Rüdiger Westermann studied computer science at the Technical University Darmstadt, Germany. He pursued his Doctoral thesis on multiresolution techniques in volume rendering, and he received a PhD in computer science from the University of Dortmund, Germany. In 2002, he was appointed the chair of computer graphics and visualization at the Technical University Munich. His research interests include scalable simulation and visualization algorithms, GPU computing, real-time rendering of large data, and uncertainty visualization.

Ole Sigmund is a Professor at the Department of Mechanical Engineering, Technical University of Denmark (DTU). He obtained his Ph.D.-degree 1994 and Habilitation in 2001 and has had research positions at University of Essen and Princeton University. He is a member of the Danish Academy of Technical Sciences and the Royal Academy of Science and Letters (Denmark) and is the former elected President (2011-15, now EC member) of ISSMO (International Society of Structural and Multidisciplinary Optimization). Research interests include theoretical extensions and applications of topology optimization methods to mechanics and multiphysics problems.